Observation of optical coupling in microdisk resonators

C. Schmidt,* A. Chipouline, T. Käsebier, E.-B. Kley, A. Tünnermann,† and T. Pertsch
Institute of Applied Physics, Friedrich-Schiller-Universität Jena, Max-Wien-Platz 1, 07743 Jena, Germany

V. Shuvayev and L. I. Deych
Department of Physics of Queens College, The City University of New York, 65-30 Kissena Boulevard, Flushing, New York 11367, USA
(Received 28 July 2009; published 30 October 2009)

In this paper, optical properties of coupled silica disk microresonators are investigated. The spectral response and the light intensity distribution along the coupled disks were measured. It was found that the distribution depends on the particular excited resonance, which can be attributed to the formation of normal modes of the coupled resonator system. A developed theoretical model gives quantitative agreement with the experimental observations.

DOI: 10.1103/PhysRevA.80.043841 PACS number(s): 42.60.Da, 42.82.Et, 42.82.Cr, 42.25.Bs

I. INTRODUCTION

Optical microresonators of different morphology (spheres, disks, toroids, pillars, and rings) have been attracting a great deal of interests in the last decade due to their potential use as building blocks in future microphotonic and nanophotonic devices [1]. These resonators support whispering gallery modes (WGMs) with extremely high Q factors (as high as 10^8 for spheres and 10^6 for disks) and very small mode volume. Recently, the focus of research in this area has shifted from individual systems [2–11] to coupled resonator structures. Due to the fact that the advantage of highest Q factors is offset by difficulties in achieving size uniformity required for coupled structures [12], coupled microspheres were mainly investigated in terms of light propagation effects depending on the size disorder of the individual spheres [13,14]. While these effects are of interest from the point of view of optical investigation of Anderson localization [15], they are detrimental for most potential applications. On the other hand, despite the lower Q factors, the advantage of disk and ring microresonators is the ability to fabricate them with the accuracy much better than for microspheres using an electron-beam lithography process. Therefore, coupled ring resonators, for instance, were investigated for such configurations and applications as coupled resonator optical waveguides (CROW) [16], side-coupled integrated spaced sequence of resonators (SCISSOR) [17], tunable filters [18], slow light devices [19], and nonlinear wavelength converters [20]. To get a better understanding of optical coupling of microresonators, scientists started to investigate microdisks and microspheres in the context of so-called "photonic molecules" [21–23], where two or only a few resonators are coupled. Based on such structures, for instance, an enhancement of the sensitivity of an integrated biosensor was theoretically predicted [24].

In this paper, we present experimental and theoretical investigations of coupled microdisk structures. We describe a manufacturing procedure for fabrication of such structures with arbitrary configurations. Experimental data of two and three coupled disks are compared with theoretical calculations based on the developed analytical model.

II. THEORETICAL MODEL

An effective theoretical description of individual and multiple disk systems is based on a two-dimensional approximation, which is valid as long as the thickness of the disks does not allow for formation of standing waves in the "vertical" (perpendicular to the plane of the disks) direction, which will be chosen to be the z axis. In this case, in-plane and vertical coordinates can be approximately separated [11,25,26] and the thickness of the disk is incorporated through the concept of an effective refractive index. In this approach, Maxwell equations are reduced to a two-dimensional scalar wave equation with an effective refractive index for z component of magnetic (TE polarization) or electric (TM polarization) fields. The effective refractive index in this approximation is different for modes of different polarizations and is better treated as a fitting parameter determined from comparison between calculated and measured resonance positions for single disks. With this approach, the two-dimensional (2D) approximation (2D model) is accurate enough to give reasonable agreement between experimental and theoretical results for coupled disks, which will be shown below.

The systems of coupled disks have been studied intensively by a variety of numerical methods (see recent review in [27] and references therein as well as [23,24,28]). These methods are based on the numerical solution of integral equations and allow studying structures of coupled disks with noncircular boundaries. However, in the experiments described in this work, the disks have almost ideal circular shape [Figs. 1(a) and 1(b)]. Taking advantage of this fact, we can use a simpler and physically more transparent approach based on modal expansion, which, in the case of high-Q whispering gallery modes, allows for additional simplifications. This approach is similar to multisphere Mie analysis [29] and its application to the case of high-Q WGMs in coupled spherical microresonators [21,30–32].

Let us consider pth disk of our structure characterized by radius R_p and position of the center $\mathbf{r}_p$. We present internal

*ca.schmidt@uni-jena.de
†Also at Fraunhofer Institute of Applied Optics and Precision Engineering Jena, Germany.

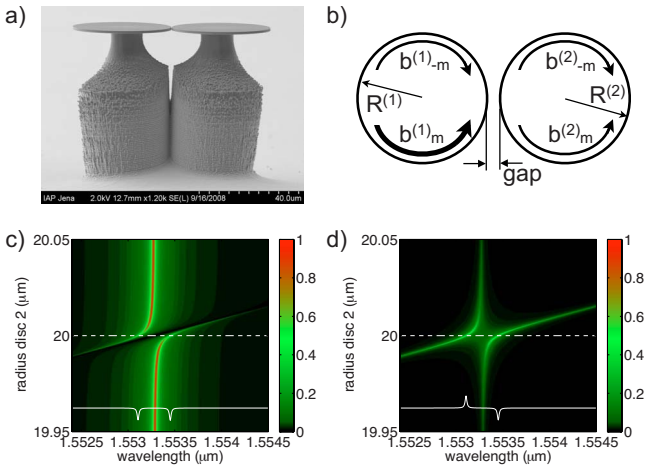

FIG. 1. (Color online) (a) shows a SEM picture of an investigated sample of two coupled disks. (b) shows the sketch of the 2D representation of the structure with notations of radii and the calculated expansion coefficients (the thick arrow marks the excited mode). The lower two pictures show the calculated spectra of the $b_{\pm 103}^{(1,2)}$ expansion coefficients for the scattered field of first (c) and second (d) disks for varying radius of second disk (single disk resonance at 1.5533 μm with $m=103$) exhibiting splitting of the resonances. The white solid lines show the real part of the coefficients along the dashed white lines for equal radii of 20 μm. In this case, light intensity is equal in both disks for both resonances.

and scattered magnetic fields (without restrictions only TE polarization is considered) associated with this disk as a linear combination of two-dimensional cylindrical harmonics with radial parts having a form of Bessel (for the inside field) or Hankel (for the scattered field) functions

$$B_{\text{int}}^{(p)} = \sum_m d_m^{(p)}(\omega) e^{im\phi_p} J_m(n_d k|\mathbf{r}-\mathbf{r}_p|), \tag{1}$$

$$B_{\text{sc}}^{(p)} = \sum_m b_m^{(p)}(\omega) e^{im\phi_p} H_m(n_0 k|\mathbf{r}-\mathbf{r}_p|). \tag{2}$$

The field incident on this disk has contributions from the original incident field as defined in the coordinate system centered at this disk plus the field scattered by all other disks

$$B_{\text{inc}}^{(p)} = \sum_m a_m^{(p)}(\omega) e^{im\phi_p} J_m(n_d k|\mathbf{r}-\mathbf{r}_p|) + \sum_{q\neq p}\sum_m b_m^{(q)} \times(\omega) e^{im\phi_q} H_m(n_0 k|\mathbf{r}-\mathbf{r}_q|). \tag{3}$$

In these equations, m is the azimuthal mode number, n_d is the effective refractive index as mentioned above, n_0 is the refractive index of surrounding media (air), and k is the vacuum wave number. Expansion coefficients $b_m^{(p)}$, $d_m^{(p)}$, and $a_m^{(p)}$ define contributions of mth mode of the pth disk to the respective fields. The polar angles ϕ_q are defined in local polar coordinate systems, which are centered at different $\mathbf{r}_p$ but have the same orientation for all disks in the structure. In order to be able to use boundary conditions at the rim of the pth disk, the scattered field [Eq. (3)] needs to be rewritten in the coordinate system centered at the pth disk. This can be achieved with the help of Grafs formula for the Hankel function [24]

$$e^{im\phi_q} H_m(n_0 k|\mathbf{r}-\mathbf{r}_q|) = \sum_{n=-\infty}^{+\infty} H_{n-m}(n_0 k R_{q,p}) e^{i(m-n)\theta_{q,p}} J_n(n_0 k|\mathbf{r}-\mathbf{r}_p|) e^{in\phi_p}, \tag{4}$$

where $R_{q,p}$ and $\theta_{q,p}$ are radial and polar coordinates of the pth disk in the coordinate system centered at the qth disk. Substituting Eq. (4) in Eq. (3) leads to

$$B_{\text{inc}}^{(p)} = \sum_m \left[a_m^{(p)}(\omega) + \sum_{q\neq p}\sum_n b_n^{(q)}(\omega) H_{m-n}(n_0 k R_{q,p}) e^{i(n-m)\theta_{q,p}} \right] \times e^{im\phi_p} J_m(n_0 k|\mathbf{r}-\mathbf{r}_p|). \tag{5}$$

Matching internal, scattered, and incident fields given by Eqs. (1)–(3), respectively, with the help of Maxwell boundary conditions, we arrive at a system of linear equations relating expansion coefficients of scattered and incident fields for different disks

$$b_m^{(p)}(\omega) = \alpha_m^{(p)}(\omega) \left[a_m^{(p)}(\omega) + \sum_{q\neq p}\sum_n b_n^{(q)} \times(\omega) H_{m-n}(n_0 k R_{q,p}) e^{i(n-m)\theta_{q,p}} \right]. \tag{6}$$

Here we introduced the single disk scattering amplitude

$$\alpha_m^{(p)}(\omega) = \frac{n_d J_m(x_d) J_m'(x_0) - n_d J_m'(x_d) J_m(x_0)}{n_0 H_m(x_0) J_m'(x_d) - n_d J_m(x_d) H_m'(x_0)}, \tag{7}$$

where $x_{0,d}=n_{0,d}kR^{(p)}$. The system of linear coupled Eqs. (6), which for two disks was obtained in [26], describes the problem in the most general form for an arbitrary configuration of disks and taking into account coupling between all azimuthal modes. In order to consider a linear chain of disks, we can choose the polar axis of the coordinate system along the line connecting disk's centers and specifying that

$$\theta_{q,p} = \begin{cases} \pi, & q > p \\ 0, & q < p. \end{cases} \tag{8}$$

In the case of high-Q whispering gallery modes, additional simplifications are possible. Indeed, in this case one deals with modes characterized by large azimuthal index $|m| \gg 1$. Since Hankel function with large indices grows exponentially with increasing $|m|$, the largest contribution to Eq. (6) comes from terms with $n=-m$, which means that a mode with a given m couples strongest to a counterpropagating mode $n=-m$ in the adjacent disk, which is characterized by the same resonance frequency. At the same time, interaction with nonresonant modes will be shown to result in qualitatively new effects, which can be accounted for perturbatively. In addition, Hankel functions with $|m| \gg 1$ decrease very fast with increasing distance between the disks (evanescent coupling), which allows treating Eq. (6) in the nearest-neighbor approximation.

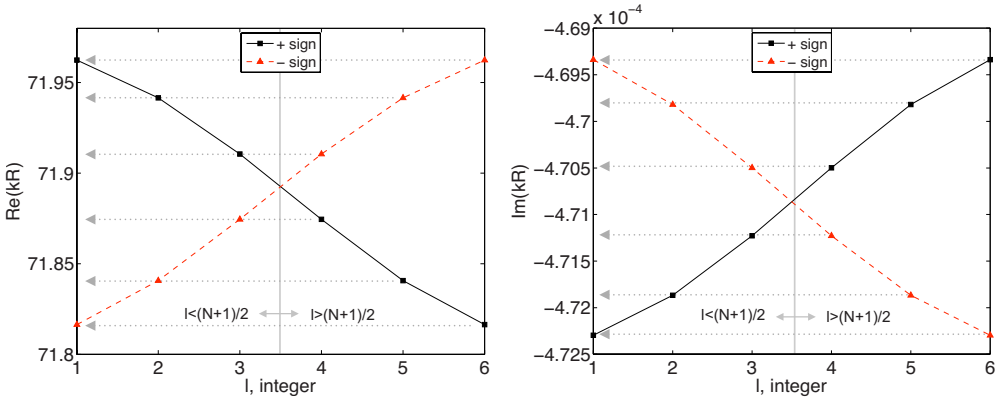

FIG. 2. (Color online) Solution of dispersion relation (13) for the case of six coupled disks, showing two branches of normal quasimodes, characterized by complex-valued frequencies [left (right) graph shows real (imaginary) part]. The dashed arrows mark the normal frequencies and the two corresponding modes from the two branches.

A. Nearest-neighbors resonant approximation

In the simplest approximation, we only take into account in Eq. (6) nearest-neighbor terms with azimuthal index $n=-m$. Taking into account that $H_{-m}(x)=(-1)^m H_m(x)$, we rewrite Eq. (6) in the following form:

$$b_M^{(p)}(\omega)=\alpha_M^{(p)}(\omega)[a_M^{(p)}(\omega)+b_{-M}^{(p-1)}(\omega)H_{2M}(n_0kR_{p-1,p})+b_{-M}^{(p+1)}(\omega)H_{2M}(n_0kR_{p+1,p})],$$

$$b_{-M}^{(p)}(\omega)=\alpha_M^{(p)}(\omega)[b_M^{(p-1)}(\omega)H_{2M}(n_0kR_{p-1,p})+b_M^{(p+1)}(\omega)H_{2M}(n_0kR_{p+1,p})], \quad (9)$$

where we assumed that the incident wave has only M azimuthal component. In a finite chain of N disks numerated from $p=1,\ldots,N$, these equations must be complemented by boundary conditions

$$b_M^{(0)}=b_{-M}^{(0)}=b_M^{(N+1)}=b_{-M}^{(N+1)}=0. \quad (10)$$

In the case of identical disks positioned at equal distances from each other, the solution of Eqs. (9) with boundary conditions [Eq. (10)] can be found using discrete sine Fourier transform. Assuming that only disk p_0 is excited, we find

$$b_{\pm M}^{(p)}=\frac{2}{N+1}\sum_{l=1}^{N}\tilde{b}_{\pm M}^{(l)}\sin\left(\frac{\pi l}{N+1}p\right), \quad (11)$$

where

$$\tilde{b}_M^{(l)}=\frac{a_M g_M(\omega)\sin\left(\frac{\pi l}{N+1}p_0\right)}{[g_M(\omega)-X][g_M(\omega)+X]},$$

$$\tilde{b}_{-M}^{(l)}=\frac{2ia_M t_M\cos\left(\frac{\pi l}{N+1}\right)\sin\left(\frac{\pi l}{N+1}p_0\right)}{[g_M(\omega)-X][g_M(\omega)+X]}, \quad (12)$$

with $X=2it_M\cos[\pi l/(N+1)]$. Here we introduced inverse single disk scattering amplitude $g_M(\omega)=[\alpha_M(\omega)]^{-1}$ and the nearest-neighbor coupling parameter for resonant modes $t_M=-iH_{2M}(n_0kD)$, which depends on the distance between the centers of the adjacent disks $D\geq 2R$, and is defined to have predominant real part. The resonances of this multidisk structure are determined by zeroes of denominators in Eq. (12),

$$g_M(\omega)=\pm 2it_M\cos\left(\frac{\pi l}{N+1}\right). \quad (13)$$

These equations define two branches of normal quasimodes of the chain characterized by complex-valued frequencies, whose dispersion curves are shown in Fig. 2. Each normal frequency corresponds to two different modes characterized by $l=p<(N+1)/2$ from one branch and $l=N+1-p>(N+1)/2$ from the other one. This means that in this approximation, coupling between disks does not remove the double degeneracy of the modes originally existing in single disks. These degenerate modes can be described by symmetric and antisymmetric combinations of coefficients b_M and b_{-M}. The obtained Eqs. (11) and (12) allow also describing distribution of the intensity along the chain. For instance, in the case of two disks, when only two modes with $l=1,2$ are possible, one finds (assuming that the first disk is excited)

$$b_M^{(1)}=\frac{a_M g_M(\omega)}{[g_M(\omega)-it_M][g_M(\omega)+it_M]};b_{-M}^{(1)}=0, \quad (14)$$

$$b_{-M}^{(2)}=\frac{ia_M t_M}{[g_M(\omega)-it_M][g_M(\omega)+it_M]};b_M^{(2)}=0, \quad (15)$$

so that the total intensity of the field is the same in both disks at both resonance frequencies defined by equations $g_M(\omega)\pm it_M=0$.

For the system of three disks, the situation is more interesting. For the total intensity of the field inside each disk, which is defined as $I_M^{(p)}=(|b_M^{(p)}|^2+|b_{-M}^{(p)}|^2)/|a_M|^2$, we obtain

$$I_M^{(1)}=\frac{1}{4}\left|\frac{g_M(\omega)}{[g_M(\omega)-Y][g_M(\omega)+Y]}+\alpha_M(\omega)\right|^2, \quad (16)$$

$$I_M^{(2)}=\frac{1}{4}\left|\frac{t_M}{[g_M(\omega)-Y][g_M(\omega)+Y]}\right|^2, \quad (17)$$

$$I_M^{(3)} = \frac{1}{4}\left| \frac{g_M(\omega)}{[g_M(\omega) - Y][g_M(\omega) + Y]} - \alpha_M(\omega) \right|^2, \quad (18)$$

with $Y = it_M/\sqrt{2}$. We can see that now there are three resonance frequencies, one of which coincides with the frequency of the single disk resonance determined by $[\alpha_M(\omega)]^{-1} = 0$. If the system is excited at this frequency, the intensity of the field in the middle disk is expected to be significantly smaller than in the other two disks because, as it is seen from Eq. (17), the response of the second disk does not have a resonance at this frequency. This can be understood by noting that the resonance at the single disk frequency is due to the excitation of the mode with $l = (N+1)/2$, for which parameter X introduced in Eq. (12) turns zero. In the case of three disks, this corresponds to $l = 2$. It is seen, however, from Eq. (11) that for the second disk in the three-disk structure ($p = 2$), the contribution of this mode vanishes. This phenomenon is illustrated below in Fig. 5.

B. Coupling to nonresonant modes

The role of coupling to nonresonant modes will be analyzed for the case of two disks, which do not have to be identical; implications of this analysis and its extension to longer structures are straightforward. We rewrite Eq. (6) separating out resonant and nonresonant modes. For the latter, we only take into account their interaction with the resonant modes while neglecting the interaction between themselves. Also, anticipating that the modes of the two-disk system should have definite parity with respect to inversion of the azimuthal number M [26], we introduce new coefficients

$$b_M^{\pm(p)} = b_M^{(p)} \pm b_{-M}^{(p)}, \quad (19)$$

where $p = 1, 2$ for disk one or two. Eliminating amplitudes of nonresonant modes, we derive two pairs of independent equations for "even" (b_M^+) and "odd" (b_M^-) modes

$$b_M^{+(1)}(s_M^{+(1)} + \nu_M^{+(2)}) = a_M + it_M b_M^{+(2)}, \quad (20)$$

$$b_M^{+(2)}(s_M^{+(2)} + \nu_M^{+(1)}) = it_M b_M^{+(1)}, \quad (21)$$

$$b_M^{-(1)}(s_M^{+(1)} - \nu_M^{+(2)}) = a_M - it_M b_M^{-(2)}, \quad (22)$$

$$b_M^{-(2)}(s_M^{+(2)} - \nu_M^{+(1)}) = -it_M b_M^{-(1)}. \quad (23)$$

Here we introduce new parameters emerging due to interaction with nonresonant modes

$$s_M^{(1,2)} = g_M^{(1,2)} + \sum_{n \neq -M} \alpha_n^{(1,2)} [t_{M-n}]^2 \quad (24)$$

and

$$\nu_M^{(1,2)} = \sum_{n \neq -M} \alpha_n^{(1,2)} t_{M+n} t_{M-n}, \quad (25)$$

where $t_{M \pm n} = -iH_{M \pm n}(n_0 kD)$. The main qualitative result of this interaction is that now we have four distinct resonance frequencies as oppose to just two, when the nonresonant modes are neglected. This means that nonresonant modes are responsible for lifting of the degeneracy between odd and even modes of a two-disk system. The four resonance frequencies in the case of identical disks are given by the following equation:

$$s^{(1,2,3,4)} = \pm \nu_M \pm it_M. \quad (26)$$

In the case of high-Q modes, when $|\nu_M| \ll |t_M|$, the four resonances described by Eq. (26) are grouped in two pairs of closely spaced doublets. In a general case of a N-disk chain, the coupling to nonresonant modes will split each of the dispersion curves described by Eq. (13) into two close branches.

From the experimental point of view, the relevance of interaction with nonresonant modes depends on observability of the respective doublets, which can be obscured by the weakness of this interaction and other effects such as surface roughness and deviation of the shape of the disks from the ideal circle. As it will be seen below, in our experiments the splitting of main resonances given by Eq. (26) into the doublets was not observed, which justifies neglecting nonresonant modes in our analysis.

We complemented the presented analytical calculations by the direct numerical solution of Eq. (6), taking into account only resonant modes but allowing for variations in the radii of the disks and the gap size between them. As an example, the calculated expansion coefficients for two coupled disks are plotted in Figs. 1(c) and 1(d) for both disks as a function of both the wavelength around a resonance at 1.5533 μm and the radius of the second disk. It can be seen that even in the presence of slight size mismatch between the disks (in the range of ± 20 nm), a splitting of frequencies is still observable.

III. FABRICATION AND EXPERIMENTAL CHARACTERIZATION OF SAMPLES

To test the applicability of the theoretical model, coupled silica disk microresonators were fabricated by an electron-beam lithography process with subsequent etching steps. Starting point was a thermally oxidized silicon wafer with a silica layer of about 1 μm thickness. On top of the silica, a chromium layer and electron-beam resist were deposited. The disk structures were defined by the electron-beam writing process. After resist development and chromium etching, the remaining chromium acts as an etching mask for the silica and the silicon below. In an anisotropic etching step, the disk structures were transferred into the silica layer. There after, the silicon was isotropically etched, which leads to an underetching of the silica layer and produces free standing silica disks on silicon pedestals. In a penultimate step, the silicon was deeply etched to get a larger distance of the silica disks to the silicon substrate in order to provide easy access for a tapered optical fiber. Finally, the chromium mask was removed.

The fabricated samples were spectrally characterized with a tunable laser source in the telecommunication band. The light from the laser was coupled through a tapered optical fiber (diameter of approximately 1.3 μm), which was brought in close proximity to the investigated disk resonators

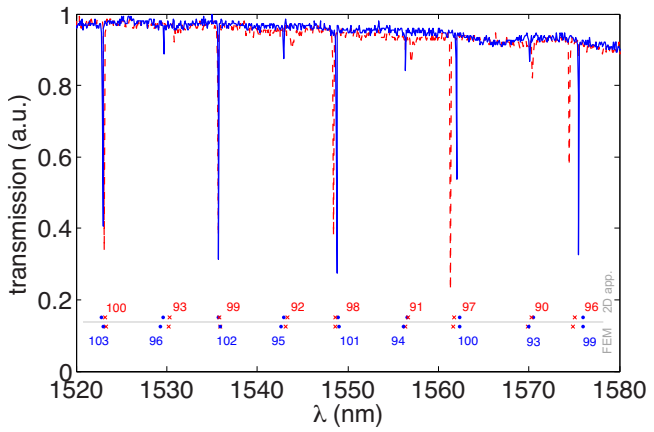

FIG. 3. (Color online) Measured spectral response of a single disk resonator for both polarization states (TE: blue solid line, TM: red dashed line). The blue dots (TE) and red crosses (TM) are the calculated resonance wavelengths [above (below) the gray line from the 2D-effective index (FEM) model] with the corresponding azimuthal mode numbers m. The stronger resonances are fundamental (high Q) modes with large m. The weaker excited resonances are second-order radial modes (two intensity maxima in radial direction) with lower values of m. Due to the good agreement for the relative distances of differently polarized modes, the measured resonances can be identified.

and provides very efficient coupling due to strong-mode field overlap and phase matching of both modes [8]. The output of the tapered fiber was then connected to a photodiode with 125 MHz bandwidth, which was connected to an oscilloscope. The laser was operated in continuous sweeping mode and when the excitation wavelength coincides with a resonance the transmission through the taper drops. Therefore, the spectral response of the disk microresonator is directly observable on the oscilloscope. The polarization of the excited resonances can be controlled with an inline fiber polarization controller. Part of the light coupled to the disk is scattered out of the disk and is collected by an infrared camera. This information is complementary to spectral data and can be used to characterize the field distribution among disks of the coupled resonator system.

First, the spectral response of a single disk resonator was measured to identify the modes in the investigated wavelength range. The measured spectra were compared with results of numerical simulations using the 2D model described above by calculating the poles of the single disk scattering amplitude [Eq. (7)]. This can be done independently for both polarizations. The refractive index n and the thickness h of the disk were used as fitting parameters. This allows us to obtain the azimuthal mode numbers as well as the polarization of the modes corresponding to the measured resonances. Due to a difference in the free spectral range of the resonances of different polarizations, the change in the polarization state of the incoming light will result in the shift of the relative positions of the observed spectral peaks. This effect is clearly seen in Fig. 3, where in the shorter wavelength range the TE resonance appears before the TM one and, at the longer wavelength range, the TE resonance appears after the TM one. The same situation can be observed in the numerical calculations and therefore with realistic choice of relevant disk parameters the polarization and mode numbers can be identified unambiguously. In this context, "realistic choice" especially restricts the thickness h of the disk, which has to be measured accurately by a scanning electron microscope (SEM). The effect of changes of h used in the simulations were investigated for the measured spectral response in Fig. 3. The depicted resonances calculated with the 2D model were obtained for $h=0.911$ μm and $n=1.451$, where h is in good agreement with the measured thickness of $h_{SEM}=(0.92\pm0.04)$ μm. Another set of parameters ($h=1.067$ μm, $n=1.443$) results in comparable agreement of the resonance wavelengths with all mode numbers increased by one, but the disk thickness in this case is significantly larger than the measured value. The same effects can be observed in results from finite element (FEM) simulations (for possible implementation, see [33]), which were used to verify our simpler two-dimensional model. The calculated resonance positions from the FEM shown in Fig. 3 below the horizontal gray line were obtained with $h=0.915$ μm, $n=1.453$, and are in good agreement with the results from the 2D model and the experimental data, especially for the fundamental modes (highest mode numbers). The difference of the disk thickness of 4 nm is clearly below the accuracy of the SEM measurement and the variations in the refractive index can be addressed to the inherent inaccuracy of the effective index method. This also explains the stronger deviations for the second-order radial modes in Fig. 3. Both the 2D effective index model and the FEM can, in principle, also be used to calculate the radiative Q factor of the disks related to the curvature of the surface (for FEM, see [33]). However, the samples under investigation show significant surface roughness, which introduces additional scattering loss as the limiting factor for the Q value. This effect cannot be easily introduced into the used models exactly and therefore the focus of this paper is not on the prediction of exact experimental Q factors. Instead, we add a small imaginary part to the refractive index to approximate all possible contributions to loss by adjusting the bandwidth of the calculated resonances to the experimental ones.

The investigated samples with two and three coupled disks show different spectral response due to a coupling-induced mode splitting, which is accompanied by a small shift of the entire spectrum. The latter might happen because of small changes in the disk parameters due to fabrication inaccuracies from sample to sample and also a change in excitation conditions. Nevertheless, the resonances still can be identified as described above if the coupling between the disks is weak, which corresponds to a large gap size between the disks.

A. Two coupled disks

For the investigation of two coupled disks, different samples were fabricated with disk radii of about 20 μm and a gap size between the disks ranging from 1 μm to 300 nm. Analog to Fig. 3, spectra were measured and, as described above, the thickness and refractive index of the disks were

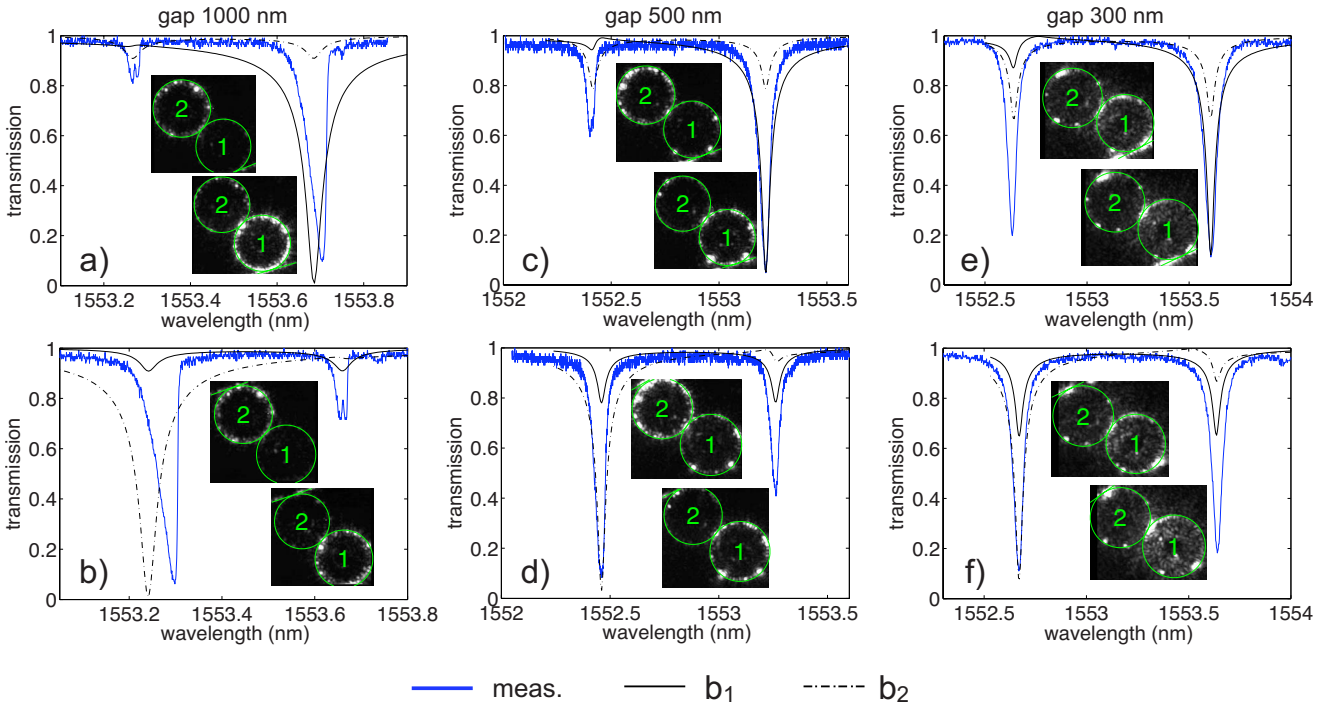

FIG. 4. (Color online) Comparison of measured resonances with theoretical calculations for two coupled disk resonators with different gap sizes (1000 nm [(a) and (b)], 500 nm [(c) and (d)], and 300 nm [(e) and (f)]). In each graph, the blue line represents the measured transmission signal through the taper. The black lines represent the calculated $1-|b_m^{(1,2)}|$, where $|b_m^{(1,2)}|$ are the normalized expansion coefficients of the scattered field of the first (solid line) and second (dashed-dotted line) disks. The insets show the images created by the infrared scattered light from both disks (the left inset in each graph corresponds to the left resonance, the right inset to the right resonance). The locations of the disks are marked by the green circles and the corresponding numbers. The tapered fiber is highlighted by a straight green line (in the upper graphs [(a), (c), and (e)] the first disk is excited; in the lower graphs [(b), (d), and (f)] the second disk is excited).

found from numerical fitting of the experimental data to be $h=1.0783$ μm and $n=1.4595$. The obtained thickness corresponds very well to measurements from SEM images of the sample, where a thickness of $h_{SEM}=(1.07\pm0.04)$ μm was found. For a detailed investigation, a TE polarized resonance with a wavelength of 1.5533 μm and an azimuthal mode number of $m=103$ were chosen. The found parameters were used in the coupled disk model to calculate the expansion coefficients $b_m^{(p)}$ of the scattered field. The wavelength dependence of these coefficients gives positions and widths of the splitted resonances, which can be compared with the experimental spectra. The magnitudes of the calculated expansion coefficients for each disk can be compared with the measured scattered light intensity. Figure 4 shows the comparison between measured and calculated data for samples with three different gap sizes. The blue line shows the measured data when the first [(a)–(c)] or second [(d)–(f)] resonator is excited; the black curves show the calculated scattering expansion coefficient (solid line for the first resonator; dashed-dotted line for the second one). For each gap size, the radius of the second resonator (R_2) was chosen to match the splitting of the resonance while the radius of the first disk was fixed to the design value for the samples ($R_1=20$ μm). For the gap sizes of 500 and 300 nm R_2 was found to be equal 19.9907 μm, while for a gap size of 1000 nm R_2 was determined to be 19.9947 μm. The difference in the radii between the samples as well as the difference between the two disks of the same sample of about 10 nm is in the range of fabrication accuracy. Within this fabrication tolerance, a direct extraction of a coupling coefficient related to the field overlap of the modes in both disks is not useful due to the fact that for each gap size different samples have to be used. To overcome this uncertainty of different samples, it would be necessary to use two initially separated disks, characterize each of them with the above-mentioned techniques, and then bring them close together with a definite but variable gap size, which from a fabrication point of view, is not easy to realize. The experimentally obtained resonance bandwidths can be reproduced, as mentioned above, by adding an imaginary part to the refractive index, which approximates all possible contributions to losses. In the simulations, it was found to be 1.5×10^{-5} and gives very good agreement for the resonance bandwidth in the case of 300 and 500 nm gap size, but for 1000 nm the calculated bandwidth is overestimated. For the latter sample with the weakest coupling between the resonators, we also observed a surface scattering-induced splitting and for the strong resonances we found a slightly nonsymmetrical broadening due to thermal nonlinearity. We did not take the nonlinear effects and scattering at surface roughness into account and, consequently, the slight disagreement between theoretical and experimental data is not surprising. The small splitting also has to be distinguished from the described splitting due to coupling to nonresonant modes (see Sec. II B). For the smaller gap sizes, the Q factor of the coupled disk system is reduced due to coupling to nonresonant modes, no thermal broadening is observable,

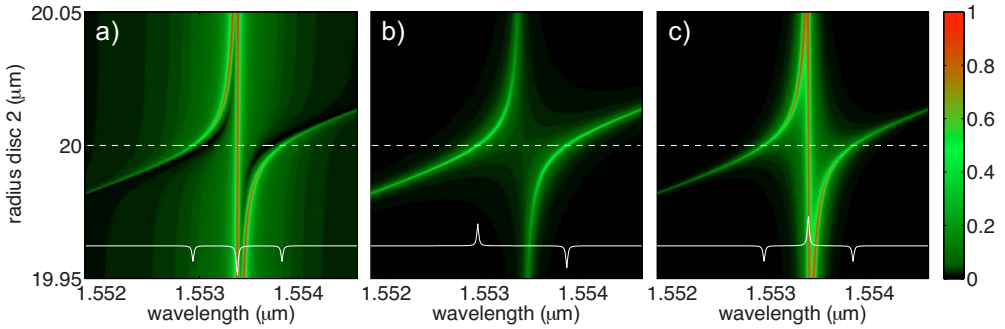

FIG. 5. (Color online) Calculated resonance splitting in the expansion coefficient for the scattered field of first (a), second (b), and third (c) disks of a linear chain of three coupled disks for varying radius of the second disk (single disk resonance at 1.553 μm with $m=103$). The white solid line in each figure shows the real part of the coefficient along the dashed white line for equal radii.

and the linear model shows very good agreement with the experimental data. The splitting is found to increase from 0.4 nm (1000 nm gap) to approximately 1 nm (300 nm gap). In accordance with theoretical predictions, the measured data show that the difference between amplitudes of the peaks in two resonators decreases with increasing coupling. The relative strength of resonances of calculated expansion coefficients for the first and second resonators manifests itself in distribution of the field intensity between the disks, as shown in the insets of Fig. 4. The upper inset corresponds to the short-wavelength resonance, whereas the lower inset represents the long-wavelength one. The green circles mark the rim of the disks, which are numbered as the first and second resonators. In Figs. 4(a) and 4(c), one can clearly see that at the shorter-wavelength resonance, the field intensity is stronger in the second resonator, while at the longer-wavelength resonance the situation is reversed. In case of excitation of the second disk instead of the first one [Figs. 4(b) and 4(d)], the distribution of intensities does not change. At the same time, the relative peak amplitudes are reversed. This asymmetry is in agreement with the theoretical calculations and is caused by slightly different resonator diameters. For a gap size of 300 nm [Figs. 4(e) and 4(f)], the measured IR signal from both of the disks could not be reproduced well by the calculated scattered field expansion coefficients. One reason for this might be the reduced difference in the coefficient strength due to the stronger coupling, which can be also seen in the measured spectra (blue curves). Another influence could arise from deposited dust and other particles at the surface of the disks, which acts as additional scattering centers and leads to a strong scattering signal randomly distributed along the rim of the disks (this fact was verified by SEM measurements after the experiment).

B. Three coupled disks

The theoretical model for the scattered field expansion coefficients [Eq. (6)] was also applied for a linear chain of three coupled disks. For comparison with the experimental data, the radius of the middle disk was used as a parameter, which is consistent with the characteristics of the fabrication process. Additionally, an imaginary part of refractive index of 10^{-5} was found to give the best fit for the bandwidth of the experimental data. In comparison to the two-disk case, the spectral positions of the resonances did not change significantly and, therefore, the refractive index and thickness of the disks as well as the mode number were taken from the two-disk calculations. In Fig. 5, the influence of radius mismatch of the second disk (disk in the middle of the structure) is plotted for a gap size of 300 nm (both gaps equal). Corresponding to the number of disks and the symmetry of the system, one can see a splitting of the resonances into three modes. Depending on the excited mode in the triplet, the intensity distribution over the disks changes. For the shortest and longest wavelengths of the splitted resonance, the field is located in all disks with the intensity maximum in the middle one (if the size of second resonator differs only weakly from the two others). For the resonance in the middle, the field is

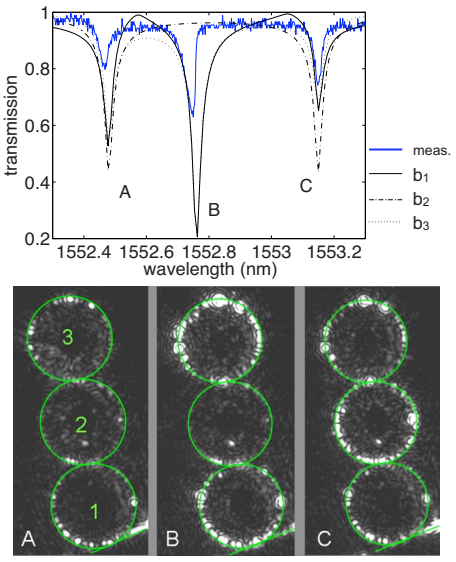

FIG. 6. (Color online) Measured spectral response of a linear chain of three coupled disks (blue line) shows splitting in three resonance dips. Good agreement can be observed for the calculated resonances (black solid line: first disk; black dashed-dotted line: middle disk; and black dotted line: third disk). For the corresponding resonances (A,B,C), the measured light distribution along the chain is plotted in the lower three figures. The relative strength of the calculated expansion coefficients $|b_m^{(1,2,3)}|$ of each disk agrees well with the measurement [especially for the middle (b) and long-wavelength (c) resonance].

only located in the first and third disks, whereas it is zero in the second one. Considering the real part of the calculated expansion coefficients, this state is an antisymmetric or odd mode of the structure with the fields having a phase shift $\pi/2$, whereas the other resonances represent symmetric or even modes with the field in all resonators in phase or π out of phase from one to another. This symmetry remains also for larger mismatches of disk radii (± 15 nm) and the fitting of the spectral position and relative distance of the three resonances could be used as a very accurate measure of the radius mismatch. The measured and calculated resonance splitting accompanied by intensity distribution is shown in Fig. 6 for the sample with a gap size of 500 nm. One can clearly see splitting into the three expected resonances. The simulation, which was done for a slightly smaller gap size of 400 nm (the real gap size is always a bit smaller than the design value due to nonvertical edges of the disks) and a radius of 20.0013 μm for the second disk, shows good agreement with the measured data. One has to mention that although the radius mismatch is very small in comparison to the deviation of gap size, it is responsible for the asymmetric splitting of resonances observed in the experiments. Also the corresponding light distribution along the chain of the disks is in a reasonably good qualitative agreement with the measured scattered light signal. Although the measured signal for the first resonance (A) is weak (only small dip in spectrum), the light is more or less equally distributed over all three disks. For the second resonance (B), the experimental data show signal only in the first and third disks, which corresponds to the calculated scattered field expansion coefficients (remember that in the spectral plots, not the expansion coefficients b_m, but $1-|b_m|$ are shown). For the third resonance (C), the light is again distributed over all disks with a stronger signal in the middle disk, which is also the case for the calculated data (stronger dip for the second disk signal at resonance C).

In conclusion, we have measured the resonance splitting and light distribution in two and three coupled disk resonators, depending on the gap size between adjacent disks. As expected, a splitting in two or three resonances has been observed for distances between the disks of less than 1 μm. The light distribution along the coupled disk structure depends on the excited resonance, which is in correspondence with the formation of normal modes of the coupled system. Comparison with the developed theoretical model shows good agreement with respect to the spectral distance of the split resonances and the light intensity distribution along the resonators. The structural parameters used for the calculations indicate a radius mismatch of the coupled disks of about 10 nm. This information can be used for very accurate measurement of the fabrication tolerances.

ACKNOWLEDGMENTS

Parts of this work were funded by the Deutsche Forschungsgemeinschaft (research unit 532) and the German Federal Ministry for Education and Research (Unternehmen Region, ZIK ultra optics).

[1] K. Vahala, Nature (London) **424**, 839 (2003).
[2] D. Armani, T. Kippenberg, S. Spillane, and K. Vahala, Nature (London) **421**, 925 (2003).
[3] M. Gorodetsky and V. Ilchenko, J. Opt. Soc. Am. B **16**, 147 (1999).
[4] S. Spillane, T. Kippenberg, and K. Vahala, Nature (London) **415**, 621 (2002).
[5] A. Smirnov, S. Rashkeev, and A. Zagoskin, Appl. Phys. Lett. **80**, 3503 (2002).
[6] C. Schmidt, A. Chipouline, T. Pertsch, A. Tünnermann, O. Egorov, F. Lederer, and L. Deych, Opt. Express **16**, 6285 (2008).
[7] S. Götzinger, O. Benson, and V. Sandoghdar, Opt. Lett. **27**, 80 (2002).
[8] B. Little, J. Laine, H. Haus, and L. Fellow, J. Lightwave Technol. **17**, 704 (1999).
[9] A. Fomin, M. Gorodetsky, I. Grudinin, and V. Ilchenko, J. Opt. Soc. Am. B **22**, 459 (2005).
[10] R. Boyd and J. Heebner, Appl. Opt. **40**, 5742 (2001).
[11] M. Borselli, T. Johnson, and O. Painter, Opt. Express **13**, 1515 (2005).
[12] Y. Hara, T. Mukaiyama, K. Takeda, and M. Kuwata-Gonokami, Phys. Rev. Lett. **94**, 203905 (2005).
[13] V. Astratov, J. Franchak, and S. Ashili, Appl. Phys. Lett. **85**, 5508 (2004).
[14] B. M. Möller, U. Woggon, and M. V. Artemyev, Phys. Rev. B **75**, 245327 (2007).
[15] A. Lagendijk and B. van Tiggelen, Phys. Rep. **270**, 143 (1996).
[16] A. Yariv, Y. Xu, R. Lee, and A. Scherer, Opt. Lett. **24**, 711 (1999).
[17] J. E. Heebner, R. W. Boyd, and Q. Han Park, Phys. Rev. E **65**, 036619 (2002).
[18] L. Tobing, P. Dumon, R. Baets, and M. Chin, Opt. Lett. **33**, 2512 (2008).
[19] J. Poon, J. Scheuer, Y. Xu, and A. Yariv, J. Opt. Soc. Am. B **21**, 1665 (2004).
[20] A. Melloni, F. Morichetti, and M. Martinelli, J. Opt. Soc. Am. B **25**, C87 (2008).
[21] L. I. Deych, C. Schmidt, A. Chipouline, T. Pertsch, and A. Tünnermann, Phys. Rev. A **77**, 051801(R) (2008).
[22] S. Ashili, V. Astratov, and E. Sykes, Opt. Express **14**, 9460 (2006).
[23] S. Boriskina, Opt. Lett. **32**, 1557 (2007).
[24] S. Boriskina, J. Opt. Soc. Am. B **23**, 1565 (2006).
[25] S. L. McCall, A. F. J. Levi, R. E. Slusher, S. J. Pearton, and R. A. Logan, Appl. Phys. Lett. **60**, 289 (1992).
[26] E. Smotrova, A. Nosich, T. Benson, and P. Sewell, IEEE J. Sel. Top. Quantum Electron. **12**, 78 (2006).
[27] A. I. Nosich, E. I. Smotrova, S. V. Boriskina, T. M. Benson, and P. Sewell, Opt. Quantum Electron. **39**, 1253 (2007).
[28] S. V. Boriskina, Opt. Express **15**, 17371 (2007).

[29] M. I. Mishchenko, L. D. Travis, and A. A. Lacis, *Scattering, Absorption, and Emission of Light by Small Particles* (Cambridge University Press, Cambridge, 2002).
[30] H. Miyazaki and Y. Jimba, Phys. Rev. B **62**, 7976 (2000).
[31] L. I. Deych and O. Roslyak, Phys. Rev. E **73**, 036606 (2006).
[32] L. I. Deych, C. Schmidt, A. Chipouline, T. Pertsch, and A. Tünnermann, Appl. Phys. B: Lasers Opt. **93**, 21 (2008).
[33] M. Oxborrow, IEEE Trans. Microwave Theory Tech. **55**, 1209 (2007).